ScanSAR mode sea ice image segmentation

LANG Wenhui[1], CHANG Cancan[1], YANG Xuezhi[1], ZHANG Jie[2], MENG Junmin[2]

1. *School of computer and Information, Hefei University of Technology, Hefei* 230009, *China*;
2. *First Institute of Oceanograghy, State Oceanic Administration, Qingdao* 266061, *China*

Abstract: Non-stationary nature of SAR images is a major obstacle to the automatic interpretation of SAR sea ice image. Incidence angle effect is one of the main factors leading to instability in the sea ice image features. Based on Radarsat-1 ScanSAR mode data, this paper proposes a new segmentation algorithm which integrates incidence angle effect correction step. Considering both the speckle noise and incidence angle effect, the regional clustering, incidence angle effect correction and region merging will be combined through the pathway starting from the pixel, region and to the large-scale area. The efficiency of the proposed method has been demonstrated on the segmentation of Baffin Bay SAR sea ice image and Gulf of Bothnia SAR sea ice image, suggesting that the segmentation accuracy has been substantially improved in contrast to area-based MRF algorithm.

Key words: synthetic aperture radar, incidence angle effect, ScanSAR mode, segmentation, sea ice

CLC number: TP751.1 **Document code:** A

Citation format: **Lang W H, Chang C C, Yang X Z, Zhang J and Meng J M. 2014. ScanSAR mode sea ice image segmentation. Journal of R emote Sensing, 1 8(1): 126 – 138 [DOI: 10.11834/jrs.20132305]**

1 INTRODUCTION

Sea ice interpretation is an important application of remote sensing system. It is essential for understanding the climate and environmental change (Johannessen, 2004) and for safe navigation of ships in waters where sea ice forms (Wilson, 2004). However, a fundamental difficulty with SAR sea ice image interpretation is the large variation of the backscatter caused by numerous environmental factors (e.g., temperature, wind, ocean currents), sea ice physical properties (e.g. surface roughness, water content) and imaging parameters (e.g., incidence angle, speckle noise, wavelength, polarization mode). The same ice types can appear quite different in SAR images of different seasons. Moreover, even within a single image, ice classes can exhibit a varying signature as a function of the incidence angle. The speckle noise results in significant confusions in extracting the intensity and texture feature of sea ice. The existing semi-a utomatic and automatic interpretation methods of SAR sea ice image, such as Finland's PCNN (Karvonen, 2004), Canadian MAGIC (Clausi, 2010) and the United States ARKTOS (Soh, 2004), usually segment the image before image classification in order to suppress speckle noise to extract high level features such as the shape and size. But all these methods only consider the l ocal nonstationarity of SAR images, and can not adapt to the large scale changes caused by incidence angle, and can not ensure the segmentation accuracy of wide swath spaceborne and airborne SAR sea ice image. Therefore, based on the Radarsat-1 ScanSAR mode data, this paper presents a segmentation algorithm which integrates incidence angle effect correction step.

Considering that the sea ice is horizontal surfaces, ice automatic interpretation system usually completes the operations such as radiation calibration, projection transform and range correction in the preprocessing stage. Range correction includes an antenna pattern correction, slant distance signal compensation as well as incidence angle correction (Johannessen, 2007). Based on the knowledge of the gain profile of antenna coil and the reciprocal of slant distance cubic, we can conveniently realize the above two corrections. However, for the distributed target, incidence angle effect usually makes the appearance of sea ice change greatly from close range (small incidence angle) to far range (large incidence angle). Radar echo is stronger at close range, and will be weakened with the moving to a far range. For example, for a sea ice SAR image acquired by RADARSAT ScanSAR in C-band, the incidence angle range is up to 27°, corresponding to the same sea ice strength change of approximately −0.20 — −0.30dB/°. For airborne SAR data, while the incidence angle changes often can reach more than 40°, so that the incidence a ngle effect is more obvious. Mäkynen, et al. (2002) has shown that this effect (the angle dependence) depends not only on the incidence angle, but also on the sea ice roughness, salt content and physical structure, namely, the sea ice types. Therefore, the Canadian sea ice Department which released the Radarsat-1 and Radarsa-2 sea ice images currently, has terminated the global c alibration services for incidence angle effect.

We believe that the incidence angle effect is a kind of image degradation. It makes the images unstable along the range, re-

Received: 2012-11-02; **Accepted:** 2013-08-23; **Version of record first published:** 2013-08-30

Foundation: National Natural Science Foundation of China (No. 61271381, No. 41076120, No. 60890075).

First author biography: LANG Wenhui (1965—), male, associate professor. His research interest are remote sensing image processing and intelligent information processing. E-mail: langwh@hfut.edu.cn

sulting in the observed image having more information than the o riginal "real" image. But it is equivalent to the real image i nformation to add additional sources of information (bias field), and different types of sea ices have different patterns of bias field. Apparently, we have known types of sea ice which are the premise of the type of correction. Sea ice segmentation is a low level classification, which makes the integrated incidence angle correction step in the segmentation process. On the other hand, the information minimization method along the range can minimize the introduced additional information in the degradation process, and thus solve two key problems: model selection and calibration parameter optimization which are required in the c orrection process.

The paper considers the speckle noise, incidence angle effects and other uncertainties in the segmentation process based on ice chart (Ma, et al., 2011) which gives the sea ice type number of designated areas. In order to improve segmentation algorithm ability to adapt to non-stationary, the regional clustering, incidence angle effect correction and region merging will be combined through the pathway starting from the pixel, to the r egion, and to the large-scale area.

2 DATA PREPARATION

2.1 Data processing

In this paper, test data used is the Radarsat-1 ScanSAR mode data. The first is the Baffin Bay image collected by R ADARSAT-1 wide ScanSAR in October 18, 2005. Its incidence angle range is 20°—49°. The ice class corresponding incidence angle is about 13°. The second is Gulf of Bothnia image collected by RADARSAT-1 narrow ScanSAR mode in February 27, 2000. Its incidence angle range is 35°—46°. The ice class corresponding incidence angle is about 9°.

The SAR images supplied by Finland Ice Service (FIS) and Canadian Ice Service (CIS) are all registered to the same projection (e. g. Mercator projection). Then antenna pattern correction, and slant range signal compensation are also applied. The relationship between the 16-bit intensity values I and the eight-bit logorithmic pixel values P of our images is

$$P = \log_B G\sqrt{I} \qquad I \geqslant 0 \tag{1}$$

where logarithmic scale $B = 1.024$, and gain factor $G = 0.16$ (Karvonen, 2004). This transformation not only reduces the a mount of data, but also converts the multiplicative speckle noise into additive.

2.2 Ground truth data

The test should be performed with additional validated data to strengthen the conclusions. This would require creation of a dditional ground-truth images. Regional ice chart from field survey is limited. CIS has provided operational ice charts for Baffin Bay, which contains sea ice concentration and type information during the study period. These digital ice charts are p rovided in a vector format and are then rasterized to the same projection as the image data before overlaying onto the source image. By grouping together similar CIS stage of development codes, ice types contained within the polygon region were aggregated into four classes: open water, uncertain smooth ice, first year ice and multi-year ice (Table 1) (Peter, 2010). The aggregation is to ensure that each class has a sufficient number of ground truth pixels since individual stage of development codes may occur in only a few pixels in the image. In addition, based on large dynamic range of backscatter characteristics over open water, the test object does not include open water portion.

Table 1 shows the CIS codes that were aggregated into each of the class names used in Baffin Bay. Stage of development codes with a period (.) after the number are distinct ice classes from those without the period.

Table 1 Stage of development codes mapped to class name

CIS phase of development code	Class name
1, 4, 5	Smooth ice
3	First year ice
7. ,8. ,9.	Multi-year ice
Open water	Open water

Regional digital ice chart is generated every week. It is the integration of a variety of data sources, including the ice surface observations, aerial and satellite reconnaissance. Agnew and Howell (2003) compared digital ice charts with passive microwave density estimation from National Aeronautics and Space Administration (NASA) Team algorithm (Cavalieri, 1999). They found that the digital ice chart is more precise representation of ice coverage during the spring-melt and fall-freeze seasons. NASA algorithm can underestimate the ice coverage between −7.1% and −32.6%.

The ground-truth image over Gulf of Bothnia was created on the same principle. The ice classes within the area include nile ice, gray ice, smooth ice and open water. For the same reason, the open water was masked.

3 SEGMENTATION ALGORITHM

Let there be n classes into which the image is segmented. Let $\boldsymbol{S}$ be a set of sites on a lattice and $s \in \boldsymbol{S}$ be a site in the l attice.

$\boldsymbol{X} = \{X_s \mid s \in \boldsymbol{S}\}$ be a set of discrete random variables forming a random field on $\boldsymbol{S}$, with each X_s taking a value from $\{1, \cdots, n\}$. X_s indicates the class that is assigned to site s.

Let $\boldsymbol{Y} = \{\boldsymbol{Y}_s \mid s \in \boldsymbol{S}\}$ be the random field on $\boldsymbol{S}$ that is realized by the observed image. Each $\boldsymbol{Y}_s$ takes on a feature vector, with each element representing the tonal value from each of the available image channels.

Let $\boldsymbol{x} = \{x_s \mid s \in \boldsymbol{S}\}$ 和 $y = \{\boldsymbol{y}_s \mid s \in \boldsymbol{S}\}$ be realizations of $\boldsymbol{X}$ and $\boldsymbol{Y}$, respectively. Based on the information contained in the image $\boldsymbol{y}$, the image segmentation algorithm must generate the segmentation image $\boldsymbol{x}$. There will be n classes in the segmentation image, denoted by disjoint regions $\boldsymbol{\Omega}_1, \cdots, \boldsymbol{\Omega}_n$, each of which contains all the pixels assigned to one class.

The flow chart of the proposed algorithm is shown in Fig. 1. The proposed method includes region expressing, region-based initial clustering, class-based incidence angle effect correction and region merging. The dotted line represents MRF (Markov Random Filed) image segmentation algorithm.

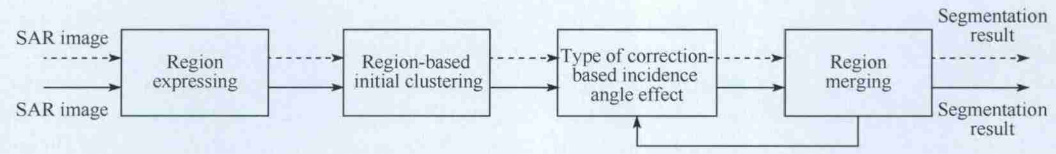

Fig.1 Flow chart of the proposed algorithm

3.1 Regional expression

The purpose of regional express is to reduce the effect of speckle noise, and identify significant homogeneous region. The concrete steps are as below.

We can use the cartoon model (Oliver,et al., 2004) that c ontains edge detection and region growth phase, assuming that images are made up of regions which reflect the local structure of image characteristics of homogeneous areas. Each region v is made up of a set of sites S_v that belongs to it. By grouping sites into regions, the effect of speckle-noise is reduced since the f eature vectors of the individual sites $\{\boldsymbol{y}_s \mid s \in \boldsymbol{S}_v\}$ can be averaged into one feature vector $\boldsymbol{y}_v$ for the entire region. On the other hand, over-segmentation characteristics in Regional expression can ensure constant incident angle, as shown in Fig. 2.

For the convenience of classification marks and region m erging, the Region Adjacency Graph (RAG) represents the s egmentation of regional adjacency relation. Each node in the graph represents a segmentation region v. The link between the nodes represents the segmented region of the common border. In the regional image, each location is no longer a single marker. Instead, all locations of the same region give the same mark. Suppose $\boldsymbol{x}^r$ represents regional images, then $\boldsymbol{X}^r$ is all possible $\boldsymbol{x}^r$ collection.

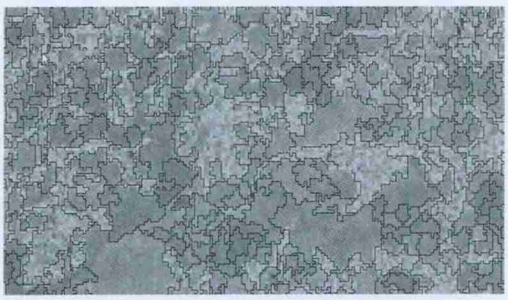

Fig.2 Regional expression of SAR sea ice images

3.2 Region-based initial clustering

In order to ensure the optimal labeling not being trapped in a local minimum, ice chart provides a designated area of sea ice type number information. Each of the obtained watershed regions v is assigned a label x_v^r via a region-based K-means algorithm. For each region v, the K-means algorithm chooses the label that best satisfied:

$$x_v^r = \arg\min_k \sum_{s \in \boldsymbol{S}_v} (\boldsymbol{y}_s - \boldsymbol{\mu}_k)^{\mathrm{T}} (\boldsymbol{y}_s - \boldsymbol{\mu}_k) \tag{2}$$

where $\boldsymbol{y}_s$ is the feature vector at site s whose elements are the values of the image channels and where T is the transpose operator. This process is iterative and begins with random means $\boldsymbol{\mu}_k$ that are updated on each iteration.

3.3 Type of correction-based incidence angle effect

Image degradation usually can be described by the linear model (Beckers, 1994). Let y^r denotes the observed tonal value corresponding to the region labelled by k and let z^r denotes the "true" tonal value. The relationship between two variables can be written as

$$y^r = z^r m^r + a^r \tag{3}$$

where m^r is a multiplicative intensity degradation factor, and a^r is an additive intensity degradation factor.

The estimation $\tilde{z}^r$ of the true image z^r is obtained by the i nverse of the degradation model

$$\tilde{z}^r = y^r (\tilde{m}^r)^{-1} + (\tilde{a}^r)^{-1} \tag{4}$$

where

$$(\tilde{m}^r)^{-1} = \frac{1}{m^r} \text{ and } (\tilde{a}^r)^{-1} = -\frac{a^r}{m^r} \tag{5}$$

It has to be noticed that the intensity decreased by incidence angle variation in SAR image only appears along range direction. Therefore, we firstly calculated the mean value $\bar{y}^r(j)$ of the image along azimuth direction i

$$\bar{y}^r(j) = \frac{1}{N_j} \sum_{i \in \boldsymbol{\Omega}} y^r(i,j) \tag{6}$$

where N_j is total number of sea ice pixels of the image column j in region $\boldsymbol{\Omega}$.

Due to any segmented region on the roughness and moisture content of ice is homogeneous, intensity variation along range direction introduced by incident angle effect is the smoothing function of the location. Hence, the multiplicative and additive degradation factor can be modeled by smoothly two order polynomials

$$(\tilde{a}^r)^{-1}(j) = \sum_{q=0}^{2} a_q \frac{j^q - b_q}{c_q} \tag{7}$$

$$(\tilde{m}^r)^{-1}(j) = \sum_{q=0}^{2} m_q \frac{j^q - d_q}{e_q} \tag{8}$$

where b_q and d_q are neutralization constants, c_q and e_q are normalization constants, a_q and m_q are parameters to be optimized, and a detailed description of the derivation of parameter is given in a ppendix.

Information (I) on any image region can be represented by Shannon entropy (H) quantitatively (Applebaum, 1996)

$$I\left[\tilde{z}^r(j)\right] = H\left[\tilde{z}^r(j)\right] = -\sum_w p(w) \log p(w) \tag{9}$$

where $p(w)$ is the probability of pixels with value w in $\tilde{z}^r(j)$. The parameters a_o and m_o are optimized by Powell's multi-d imensional directional set method and Brent's one-dimen-sional optimization algorithm (Press, et al., 1992) as

$$\{a_o, m_o\} = \arg\min_{\{a,m\}} \left\{ I\left[\bar{y}(j)(\tilde{m}^r)^{-1}(j) + (\tilde{a}^r)^{-1}(j)\right] \right\} \tag{10}$$

The optimal one-dimensional correction factors $(\tilde{a}^r)^{-1}(j)$ and $(\tilde{m}^r)^{-1}(j)$ are calculated from the optimal parameters a_o and

m_o, and extended to two-dimensional correction factor $(\tilde{a}^r)^{-1}(j)$ and $(\tilde{m}^r)^{-1}(j)$. Here, each row of $(\tilde{a}^r)^{-1}$ is the same as $(\tilde{a}^r)^{-1}(j)$, and each row of $(\tilde{m}^r)^{-1}$ is the same as $(\tilde{m}^r)^{-1}(j)$. The O ptimal estimation $\tilde{z}_o^r$ of "true" image z^r can be calculated using Eq.(4). Finally, regional feature vector $\boldsymbol{y}_v$ was recalculated based on the corrected results.

3.4 Region merging

After class-based incidence angle effect correction, there are still too many segmentation regions, and the adjacent regions still have various remnants of uncertainty. In addition, in the field of SAR sea ice monitoring people are more interested in the large scale ice class structures, so the region merging is necessary.

Assuming that the class value corresponding to each small region follow multivariate Gauss distribution (Press, 2007), the optimal segmentation x_o^r can be obtained by minimizing the f ollowing cost function

$$x_o^r = \arg\min_{x^r \in \boldsymbol{X}^r} E_f \tag{11}$$

where E_f is the feature model energy. E_f is defined as

$$E_f = \frac{1}{2}\sum_{k=1}^{n}\sum_{S_v \subseteq \boldsymbol{\Omega}_k}\sum_{s\in \boldsymbol{S}_v}\left\{\log\left(\left|\sum\nolimits_k\right|\right) + \left(\tilde{z}_{os}^r - \boldsymbol{\mu}_k\right)^{\mathrm{T}}\sum_k^{-1}\left(\tilde{z}_{os}^r - \boldsymbol{\mu}_k\right)\right\} \tag{12}$$

where $\tilde{\boldsymbol{z}}_{os}^r$ is the feature vector at site s, S_v are the sites in each watershed region v, and v is a part of the region $\boldsymbol{\Omega}_k$ that is a ssigned to class k. $\boldsymbol{\Sigma}_k$ is the class covariance matrix of class k and $\boldsymbol{\mu}_k$ is the mean value of class k.

Lu (2011) proposed a method for solving the Eq.(11). After the labeling process is completed for all nodes, region merging is performed in a greedy fashion. The process only considers all pairs of adjacent regions which have the same class. The algorithm will update RAG.

When region-merging is completed, the algorithm will go back to the Section 3.3 until the desired number of iterations is reached, and completes the final segmentation.

3.5 Evaluation criteria

Overall accuracy and Kappa coefficient give distinct measurements of segmentation accuracy. The overall accuracy is the percent of pixels correctly segmented. Prior to computing Kappa coefficient, the segmented results are relabeled to match the ground-truth image labels to maximize overall accuracy. The Kappa coefficient is defined as below.

$$k = \frac{P(A) - P(E)}{1 - P(E)} \tag{13}$$

where $P(A)$ is the overall classification accuracy, $P(E)$ is the desired classification accuracy. When the coefficient are located in [0.41, 0.6] interval, it is medium consistency. When the coefficients are located in [0.61, 0.8] interval, it is largely the same. When the coefficient is greater than 0.8, it is almost the same.

4 EXPERIMENT RESULT AND ANALYSIS

In order to validate the adaptation of proposed method to incidence angle effect, we divided the sea ice scene into three equal sections. Fig.3(a) is the Baffin Bay SAR sea ice image with resolution of 882×1730. Each section has a resolution of 615×938. Fig.4(a) is a Bosnian Bay SAR sea ice image with resolution of 615×938 and each section has a resolution of 205×938.

Based on the overall accuracy and kappa coefficient, the results of the proposed method were compared to that of region-based MRF. The segmentation accuracy comparisons of the experimental and sectional Baffin Bay SAR sea ice image are shown in Table 2. For the sectional image, the overall accuracy of region-based MRF is up to 89.93%, and the overall accuracy of the proposed method increased by 2.26% (92.19%—89.93%). Kappa coefficient also increased by 0.0272 (0.9087—0.8815). As for the experimental image, because of the larger effect of incidence angle effect and other nonstationary factors, the overall accuracy of region-based MRF dropped to 73.84%. The overall accuracy of the proposed method increased to 80.64% and Kappa

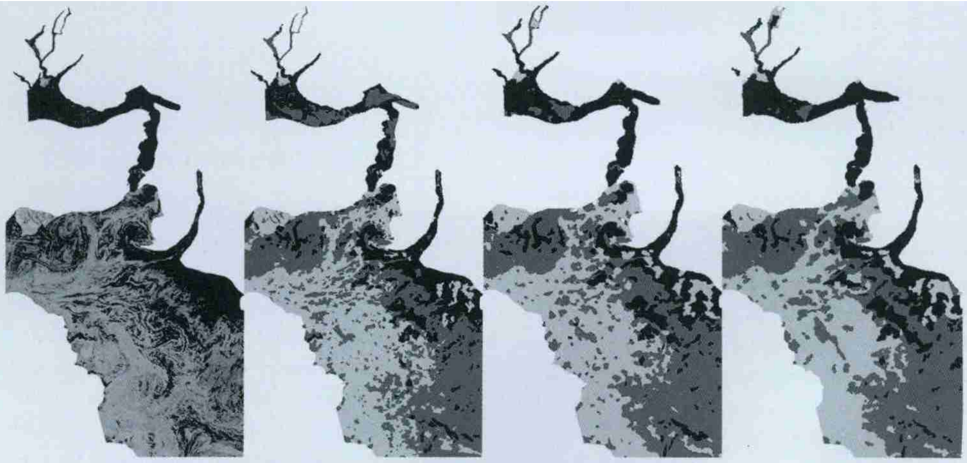

(a) Original SAR image (b) Based on the regional MRF segmentation results (c) The proposed algorithm of segmentation results (d) Ground-trut

First year ice Multi-year ice Smoothed ice

Fig.3 Baffin Bay SAR sea ice image segmentation results coefficient increased from 0.7188 to 0.7824.

In Table 3, segmentation accuracy comparisons of the e xperimental and sectional Gulf of Bothnia SAR sea ice image showed the same improvement. Unlike Baffin Bay SAR sea ice image the overall accuracy of the proposed method is the highest (95.50%—93.72%) and the Kappa coefficients improved by 0 .0169 for the sectional image. It is not that evident compared to results of Baffin bay. For the experimental image, the overall a ccuracy improved by 8.23% (86.83%—78.60%) and the Kappa coefficient increased by 0.0865.

In addition, by the comparison between Table 2 and Table 3, we found that the overall accuracy and Kappa coefficient of the Gulf of Bothnia are higher than those of Baffin Bay in the experimental resolution image and the section image. It is the likely that the range of incidence angle in Gulf of Bothnia sea ice is lower than that of Baffin Bay sea ice.

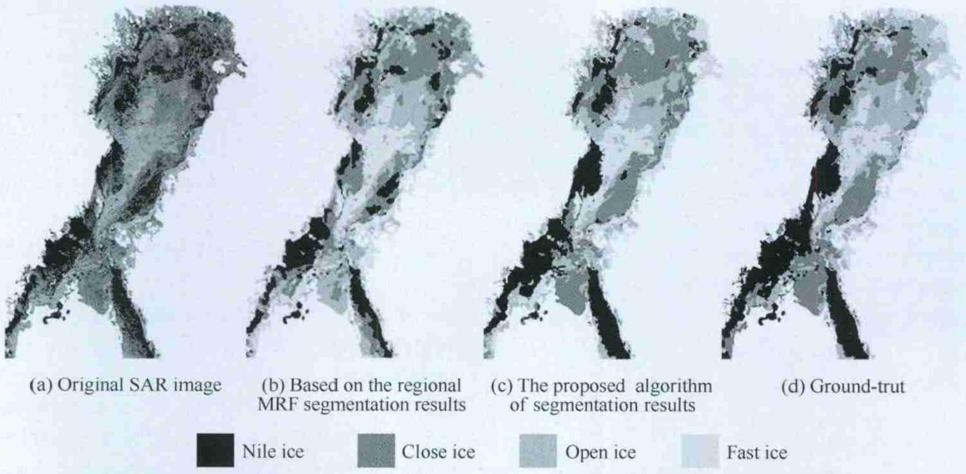

Fig.4 Gulf of Bothnia SAR sea ice image segmentation results

Table 2 Segmentation accuracy comparisons of the experimental and sectional Baffin Bay SAR sea ice image

Resolution	Region-based MRF the overall accuracy rate/%	The proposed method of the overall ccuracy rate/%	Region-based MRF of Kappa coefficient	The proposed method of Kappa coeffient
882 × 1730	73.84	80.64	0.7188	0.7824
Left 294 × 1730	80.81	81.33	0.7992	0.8016
Middle 294 × 1730	89.93	92.19	0.8815	0.9087
Right 294 × 1730	88.17	90.38	0.8623	0.8863

Table 3 Segmentation accuracy comparisons of the experimental and sectional Gulf of Bothnia SAR sea ice image

Resolution	Region-based MRF the overall accuracy rate/%	The proposed method of the overall ccuracy rate/%	Region-based MRF of Kappa coefficient	The proposed method of Kappa coeffient
615 ×938	78.60	86.83	0.7637	0.8502
Left 205 ×938	92.06	93.61	0.9082	0.9228
Middle 205 ×938	93.72	95.50	0.9144	0.9313
Right 205 ×938	85.82	85.88	0.8471	0.8478

For Baffin Bay SAR sea ice image, region-based MRF s egmentation results (Fig.3(b)) showed more ambiguity, especially the section on the right. But the proposed method (Fig.3 (c)) in these areas can achieve better edge location and regional consistency. For Gulf of Bothnia SAR sea ice image, the homogeneous sea ice pixels in the segmented image by our algorithm are more concentrated than the segmented image by region-based MRF method. In our segmented image, the area of the same kind of sea ice has better connectedness and less isolated pixels than r egion-based MRF's. Besides, the segmentation of the image by our algorithm is most likely to the ground truth, especially in left and middle sections. The result is the same to Table 2 and Table 3.

Therefore, the proposed algorithm in this paper by the integration of incident angle effect according to correction step can effectively smooth the sea ice pixels intensity values and improves the segmentation accuracy. However, with the increase of incident angle range, the improved amplitude decreased.

5 CONCLUSION AND PROSPECT

Wide swath (eg. ScanSAR technique) is a common operational sea ice monitoring mode. A major obstacle with ScanSAR sea ice image interpretation is incidence angle effect. The p roposed method integrates incident angle effect correction into the regional growth iterative from the pixel, to the region and to the large-scale area. The efficiency of the proposed method has been demonstrated on the segmentation of Baffin Bay ScanSAR sea ice image and Gulf of Bothnia ScanSAR sea ice image, where the segmentation accuracy has been substantially improved in contrast to area-based MRF algorithm. Therefore, the proposed method is suitable for unsupervised low-level classification tasks of ScanSAR sea ice images.

In addition, the optimal coefficients a_0 and m_0 as class-scale features achieved by the first combination of iteration reflect v arying tendency of the same ice class along range direction. Some studies have shown that this trend (incidence angle effect) is related to ice classes. Therefore, in future studies, we will validate the effectiveness of these features for enhancing the recognition capabilities of various types of sea ice in the high level classification.

REFERENCES

Agnew T and Howell S. 2003. The use of operational ice charts for evaluating passive microwave ice concentration data. Atmosphere-Ocean, 41(4): 317 – 331 [DOI: 10.3137/ao.410405]

Applebaum D. 1996. Probability and Information: An Integrated Approach. Cambridge: Cambridge University Press: 97

Beckers A L D, de Bruijn W C, Gelsema E S, Cleton-Soteman M I and van Eijk H G. 1994. Quantitative electron spectroscopic imaging in bio-medicine: methods for image acquisition, correction and analysis. Journal of Microscopy, 174(3): 171 – 182 [DOI: 10.1111/j.1365 – 2818.1994.tb03465.x]

Cavalieri D J, Parkinson C L, Gloersen P, Comiso J C and Zwally H J. 1999. Deriving long-term time series of sea ice cover from satellite passive-microwave multisensor data sets. Journal of Geophysical Research, 104 (C7): 15803 – 15814 [DOI: 10.1029/1999JC900081]

Clausi D A, Qin K, Chowdhury M S, Yu P and Maillard P. 2010. MAGIC: MAp-Guided Ice Classification system for operational analysis. Canadian Journal of Remote Sensing, 36(1): S13 – S25 [DOI: 10.1109/PRRS.2008.4783172]

Johannessen O M, Bengtsson L, Miles M W, Kuzmina S I, Semenov V A, Alekseev G V, Nagurnyi A P, Zakharov V F, Bobylevv L P, Pettersson L H, Hasselmann K and Cattle H P. 2004. Arctic climate change: observed and modelled temperature and sea-ice variability. Tellus-Series A-Dynamic Meteorology and Oceanography, 56 (4): 328 – 341 [DOI: 10.1111/j.1600 – 0870.2004.00060.x]

Johannessen O M, Alexandrov V, Frolov I Y, Sandven S, Pettersson L H, Bobylev L P, Kloster K, Smirnov V G, Mironov Y U and Babich N G. 2007. Remote Sensing of Sea Ice in the Northern Sea Route: Studies and Applications. Chichester: Springer-Praxis Publishing.

Karvonen A J. 2004. Baltic Sea ice SAR segmentation and classification using modified pulse-coupled neural networks. IEEE Transactions on Geoscience and Remote Sensing, 42(7): 1566 – 1574 [DOI: 10.1109/TGRS.2004.828179]

Lu J, Yang X Z, Lang W H, Zuo M X and Xu Y. 2011. SAR image segmentation with region-based GMM. Journal of Image and Graphics, 16(11): 2088 – 2094

Ma C G, Wu Y X, Shi K and Liu D G. 2011. The Internet high latitude ice information identification. Marine Technology, (2): 16 – 18

Mäkynen M P, Manninen A T, Similä M H, Karvonen A J and Martti T H. 2002. Incidence angle dependence of the statistical properties of C-Band HH-Polarization backscattering signatures of the Baltic sea ice. IEEE Transactions on Geoscience and Remote Sensing, 40 (12): 2593 – 2605 [DOI: 10.1109/TGRS.2002.806991]

Oliver C and Quegan S. 2004. Understanding Synthetic Aperture Radar Images. Raleigh: SciTech Publishing Inc: 197

Peter Y. 2010. Segmentation of RADARSAT-2 Dual-Polarization Sea Ice Imagery. Waterloo: University of Waterloo: 19 – 20

Press W H, Flannery B P, Teukolsky S A, and. Vetterling W T 1992. Numerical Recipes in C, the Art of Scientific Computing 2nd ed. Cambridge: Cambridge University Press: 402 – 419

Press W H, Teukolsky S A, Vetterling W T and Flannery B P. 2007. Numerical Recipes: the Art of Scientific Computing 3rd edn. Cambridge: Cambridge University Press: 842

Richards J A and Jia X P. 2006. Remote Sensing Digital Image Analysis. Berlin Heidelberg: Springer-Verlag: 304 – 305

Soh L K, Tsatsoulis C, Gineris D and Bertoia C. 2004. ARKTOS: An intelligent system for SAR sea ice image classification. IEEE Transactions on Geoscience and Remote Sensing, 42(1): 229 – 248 [DOI: 10.1109/TGRS.2003.817819]

Wilson K J, Falkingham J, Melling H and Abreu R D. 2004. Shipping in the Canadian Arctic: other possible climate change scenarios // Proceedings of the IEEE International Geoscience and Remote Sensing Symposium, Honolulu, Hawaii: IEEE, 3: 1853 – 1856 [DOI: 10.1109/IGARSS.2004.1370699]

Yu Q Y and Clausi D A. 2007. SAR sea ice image analysis based on iterative region growing using semantics. IEEE Transaction on Geoscience and Remote Sensing, 45(12): 3919 – 3931 [DOI: 10.1109/TGRS.2007.908876]

APPENDIX A

To neutralize the global transformation effect of the correction component $(\tilde{m}^r)^{-1}(j)$ and $(\tilde{a}^r)^{-1}(j)$ with respect to the mean value $\bar{y}^r(j)$, we introduce the mean-preserving condition as

$$\sum_{j\in\boldsymbol{\Omega}} \bar{y}^r(j) = \sum_{j\in\boldsymbol{\Omega}} \left(\bar{y}^r(j)(\tilde{m}^r)^{-1}(j) + (\tilde{a}^r)^{-1}(j)\right) \quad (A1)$$

To satisfy the above conditions, the additive factor mean value is set to 0.

$$\sum_{j\in\boldsymbol{\Omega}} (\tilde{a}^r)^{-1}(j) = 0 \quad (A2)$$

Thus the multiplicative factor should satisfy:

$$\sum_{j\in\boldsymbol{\Omega}} \bar{y}^r(j) = \sum_{j\in\boldsymbol{\Omega}} \bar{y}^r(j)(\tilde{m}^r)^{-1}(j) \quad (A3)$$

From Eq. (A2) and Eq. (7) we obtain

$$\sum_{j\in\boldsymbol{\Omega}} \left(\sum_{q=0}^{2} a_q \frac{j^q - b_q}{c_q}\right) = 0 \quad (A4)$$

From Eq. (8) and Eq. (A3) we obtain

$$\sum_{j\in\boldsymbol{\Omega}} \bar{y}^r(j) = \sum_{j\in\boldsymbol{\Omega}} \bar{y}^r(j)\left(\sum_{q=0}^{2} m_q \frac{j^q - d_q}{e_q}\right) \quad (A5)$$

First, in order to solve Eq. (A4), a_0 is set to neutral value 0

$$\sum_{j\in\boldsymbol{\Omega}} \left(\sum_{q=1}^{2} a_q \frac{j^q - b_q}{c_q}\right) = \sum_{q=1}^{2} \frac{a_q}{c_q} \sum_{j\in\boldsymbol{\Omega}} (j^q - b_q) = 0 \quad (A6)$$

when $a_q \neq 0$ and $c_q \neq 0$, now $q = 1, 2$ and we have Eq. (A7).

$$\sum_{j\in\boldsymbol{\Omega}} (j^q - b_q) = 0 \quad (A7)$$

which yields Eq. (A8)

$$b_q = \frac{1}{S}\sum_{j\in\boldsymbol{\Omega}} j^q \quad (A8)$$

where $S = \sum_{j\in\boldsymbol{\Omega}} 1$, S is the amount of pixels belong to $\boldsymbol{\Omega}$ in $\bar{y}^r(j)$. Similarly, the m_0 is set to neutral value 1

$$d_q = \sum_{j\in\boldsymbol{\Omega}} \bar{y}^r(j) j^q \Big/ \sum_{j\in\boldsymbol{\Omega}} \bar{y}^r(j) \quad (A9)$$

In order to ensure the polynomial coefficients of the same change can produce equivalent intensity changes, we normalized processing parameters

$$\frac{1}{S}\sum_{j\in\boldsymbol{\Omega}} \left| \bar{y}^r(j) \frac{j^q - d_q}{e_q} \right| = 1 \quad (A10)$$

which yields Eq. (A11)

$$e_q = \frac{1}{S}\sum_{j\in\boldsymbol{\Omega}} \left| \bar{y}^r(j)(j^q - d_q) \right| \quad (A11)$$

Similarly, we can obtian

$$c_q = \frac{1}{S}\sum_{j\in\boldsymbol{\Omega}} \left| j^q - b_q \right| \quad (A12)$$

ScanSAR 模式海冰图像的分割

郎文辉[1],常灿灿[1],杨学志[1],张杰[2],孟俊敏[2]

1. 合肥工业大学计算机与信息学院,安徽 合肥 230009;
2. 国家海洋局第一海洋研究所,山东 青岛 266061

摘 要: 合成孔径雷达 SAR(Synthetic Aperture Radar)图像的非平稳性是 SAR 海冰图像自动解释的主要障碍,入射角效应是导致海冰图像特征不稳定的主要因素之一。基于 Radarsat-1 ScanSAR 模式数据,本文提出了一种集成入射角效应校正步骤的分割算法。该方法综合考虑了入射角效应、斑点噪声等不确定因素,经由像素到区域再到大尺度区域这一途径,把区域聚类、类尺度上的入射角效应校正以及区域合并等操作组合起来,以有效提高分割算法对非平稳性的适应能力。针对巴芬湾和波斯尼亚湾 ScanSAR 模式图像的实验表明,本文提出的方法可有效提高分割准确性。

关键词: 合成孔径雷达,入射角效应,ScanSAR 模式,分割,海冰

中图分类号: TP751.1 **文献标志码:** A

引用格式: 郎文辉,常灿灿,杨学志,张杰,孟俊敏.2014.ScanSAR 模式海冰图像的分割.遥感学报,18(1):126-138

Lang W H, Chang C C, Yang X Z, Zhang J and Meng J M. 2014. ScanSAR mode sea ice image segmentation. Journal of Remote Sensing, 18(1): 126-138 [DOI: 10.11834/jrs.20132305]

1 引 言

海冰解译对理解气候与环境变化(Johannessen 等,2004)和船舶安全导航(Wilson 等,2004)具有重要意义。然而,受海冰物理特性(表面粗糙度、含水量等)、环境因素(温度、有风条件、洋流)和成像参数(入射角、相干斑噪声、波长、极化模式)的影响,相同的冰类在不同季节的 SAR 图像中可能呈现出不同的外貌。即使在单幅图像中,冰类也会呈现出与入射角相关的大尺度区域变化特征;而斑点噪声则在强度和纹理特征的提取中产生明显的混淆。现有的 SAR 海冰图像半自动和自动解译方法,如芬兰的 PCNN(Karvonen,2004),加拿大的 MAGIC(Clausi 等,2010),美国的 ARKTOS(Soh,2004)等,为了抑制斑点噪声和提取高级分类知识如形状和大小等,通常都在分类前对图像进行分割。但所有这些方法都只考虑了 SAR 图像中的局部非平稳性,而对入射角效应这样的大尺度变化,适应性较差,无法保证宽观测带星载和机载 SAR 海冰图像的分割精度。为此,基于 Radarsat-1 ScanSAR 模式数据,本文提出了一种集成入射角效应校正步骤的分割算法。

考虑到海冰为水平表面,因此海冰自动解译系统通常只需要在预处理阶段完成辐射标定、投影变换和距离校正等操作。其中距离校正包括天线方向图校正、斜距信号补偿以及针对入射角效应的校正(Johannessen 等,2007)。基于天线加感线圈的增益轮廓知识和斜距立方的倒数可方便实现对前两者的校正。然而,对分布式目标而言,入射角效应通常会引起海冰的外貌从近距(小入射角)到远距(大入射角)出现较大变化。即雷达回波在近距较强,随着向远距移动将逐渐减弱,例如一幅由 RADARSAT ScanSAR 在 C-band 采集的海冰 SAR 图像,其入射角变化范围可达 27°,对应的同类海冰强度变化大约为 -0.20 — -0.30 dB/°(Mäkynen 等,2002);而对机载 SAR 数据来说,入射角的变化往往能达到 40°以上,入射角效应更为明显。Mäkynen 等人(2002)的研究表明,这种效应(角度依赖性)不仅取决于入射角,而且取决于海冰的粗糙度、含水量和物理结构,即海冰类型。因此,加拿大海冰署在目前发布的 Radarsat-1/2 海冰图像中,已经终止

收稿日期:2012-11-02;修订日期:2013-08-23;优先数字出版日期:2013-08-30

基金项目:国家自然科学基金(编号:61271381,41076120,60890075)

第一作者简介:郎文辉(1965—),男,副教授。主要研究方向为遥感图像处理,智能信息处理,已发表论文三十余篇。E-mail: langwh@hfut.edu.cn

了针对入射角效应的全局校正服务。

入射角效应是一种图像退化效应,它使图像沿距离向处于一种不稳定状态,客观上造成观测图像的信息多于原来的“真实”图像,相当于在真实图像信息上增加了附加的信息源(偏差场),且不同类型的海冰具有不同模式的偏差场。显然,按类校正的前提是已知海冰类型,而海冰分割本质上是对海冰的低级分类,这为在分割过程中集成入射角校正步骤提供了可能。另一方面,沿距离向的信息最小化方法可以最大程度地减少退化过程引入的附加信息,解决了校正过程所需的模型选择和校正参数寻优两个关键问题。

本文综合考虑斑点噪声、入射角效应等不确定因素,在分割过程中基于冰况图(马闯关 等,2011)给出的指定区域海冰类型数量信息,经由像素到区域再到大尺度区域这一途径,把区域聚类、类尺度上的入射角效应校正以及区域合并等操作组合起来,以有效提高分割算法对非平稳性的适应能力。

2 数据准备

2.1 数据处理

本文使用的试验数据是 Radarsat-1 ScanSAR 模式数据。第 1 幅是由 Radarsat-1 宽幅 ScanSAR 模式于 2005 年 10 月 18 日采集的巴芬湾(Baffin Bay)图像,入射角变化范围 20°—49°,其中冰类对应的入射角范围约为 13°。第 2 幅测试图像由 Radarsat-1 窄幅 ScanSAR 模式于 2000 年 2 月 27 日在波罗的海的波斯尼亚湾(Gulf of Bothnia)上空采集,入射角变化范围 35°—46°,其中冰类对应的入射角跨度约为 9°。

上述两幅图像分别由芬兰冰中心 FIS(Finnish Ice Service)和加拿大海冰署 CIS(Canadian Ice Service)提供,均已完成投影重采(如墨卡托投影)、天线方向图校正和斜距信号补偿。8-位图像像素值 P 与 16-位原始强度值 I 之间的关系为

$$P = \log_B G\sqrt{I} \qquad I \geqslant 0 \tag{1}$$

式中,$B=1.024$,增益因子 $G=0.16$(Karvonen,2004)。在满足分辨率要求的同时,这种变换不仅减少了数据量,而且把乘性斑点噪声转换为加性。

2.2 地面实况图

为方便比较,需要制作这两幅图像的地面实况图。由于实地考察困难,我们参考了相关区域的同期冰况图。加拿大海冰署(CIS)制作的同期冰况图涵盖了巴芬湾的海冰密集度和类型信息。由于冰况图是以矢量多边形的形式提供的,因此在与源图像叠加前,先将其光栅投影为图像格式。在重叠后的多边形区域中,通过组合 CIS 定义的成冰阶段代码,把巴芬湾对应的冰类归类为 4 类:敞水、不确定的平滑冰、初期冰和多年冰(Peter,2010),如表 1 所示。由于某些成冰阶段代码只与图像中的少量像素对应,因此完成这种映射可以保证每一冰类有足够数量的地面真实像素。此外,基于敞水的高动态后向散射特性,测试对象未包括敞水部分,因此对其施加了掩模。

表 1 给出了成冰阶段代码与巴芬湾海冰类型间的映射。带有(.)的成冰阶段代码与不带的代码代表不同的冰类。

表 1　成冰阶段代码对应的类名

CIS 形成阶段代码	类名
1,4,5	不确定平滑冰
3	初期冰
7.,8.,9.	多年冰
敞水	敞水

区域数字冰况图每周生成一幅,它是各种数据源的信息融合,包括冰面观测、空中和卫星侦察。Agnew 和 Howell(2003)曾把 CIS 数字冰况图与美国 NASA(National Aeronautics and Space Administration)的被动微波密集度估计算法(Cavalieri 等,1999)进行了比较,发现在春融和秋冻季节,NASA 算法对海冰密集度的低估可达 −7.1% 到 −32.6%,而 CIS 数字冰况图则能更精确地表示海冰密集度。因此,基于所有可用信息,冰况图代表了某时段冰况的最佳估计,而据此制作的地面实况图,其精度是可信的。

波斯尼亚湾的地面实况图也是采用同样原理制作的。该区域中的冰类包括:尼罗冰、密集冰和稀疏冰和固定冰(Mäkynen 等,2002)。由于同样的原因对敞水施加了掩模。

3 分割算法

假设把图像分为 n(冰)类,S 是栅格上的一组位置,$s \in S$ 是栅格中的某个位置。

$X = \{X_s | s \in S\}$ 是一组离散的随机变量,在 S 上构成了一个随机场,每个 X_s 从 $\{1,\cdots,n\}$ 中取一

个值。X_s 表示赋值给位置 s 的(冰)类。

$Y = \{Y_s | s \in S\}$ 也是 S 上的随机场,Y_s 是位置 s 处的与观测值有关的特征矢量,如某个 SAR 图像通道的亮度。

假设 $x = \{x_s | s \in S\}$ 和 $y = \{y_s | s \in S\}$ 分别是 X 和 Y 的随机实例。基于图像 y 中包含的信息,图像分割算法必定产生分割图像 x。在分割图像中将有 n 类,由不相连的区域 $\Omega_1,\cdots,\Omega_n$ 表示,每个区域中的像素具有相同的类标记。

图 1 给出了所提方法的主要步骤,包括:区域化表示、初始聚类、入射角效应按类校正和区域合并。虚线代表了未包括入射角效应校正步骤的分割流程(Yu 和 Clausi,2007),称之为基于区域 MRF (Markov Random Field)的图像分割算法。

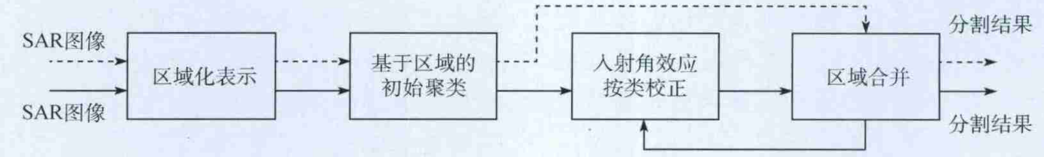

图 1 算法流程图

3.1 区域化表示(结构去噪)

区域化表示的目的是消除雷达图像的噪声影响,并识别显著的同质区域。具体步骤如下:

首先利用卡通模型(Oliver 和 Quegan,2004),经由边缘检测和区域生长阶段,把图像分割成许多小的反映图像局部结构特征的同质区域。然后,每个区域 v 由一组属于该区域的位置 S_v 构成,通过把各位置的特征矢量$\{y_s | s \in S_v\}$平均到一个区域特征矢量 y_v,可以有效降低斑点噪声,称为结构去噪。区域化过程的过分割特性,也可以保证入射角的渐变性,如图 2 所示。

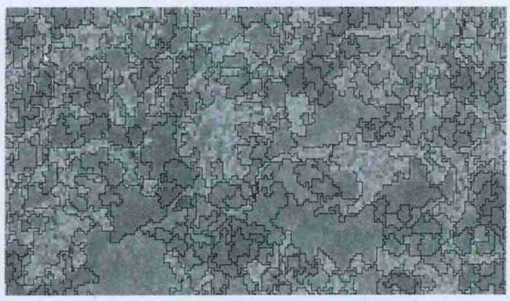
图 2 SAR 海冰图像的区域化表示

为方便分类标记和区域合并,采用了区域邻接图 RAG(Region Adjacency Graph)这种数据结构来表征分割区域间的邻接关系。邻接图中的每个节点代表一个分割区域 v,节点之间的链接代表分割区域间存在的共同边界。在区域化图像中,每个位置不再有单独的标记。取而代之,把同一区域中的所有位置赋予同一标记。假设 x^r 代表区域化后的图像,则 X^r 是所有可能的 x^r 集合。

3.2 基于区域的初始聚类

为保证标记寻优过程不陷入局部极值,将基于冰况图提供的指定区域海冰类型数量信息,采用区域 K-均值算法,把标记 x_v^r 赋予所获得的每一分割区域 v。即针对每个区域 v,找出最符合下式的标记:

$$x_v^r = \arg\min_k \sum_{s \in S_v} (\boldsymbol{y}_s - \boldsymbol{\mu}_k)^{\mathrm{T}} (\boldsymbol{y}_s - \boldsymbol{\mu}_k) \tag{2}$$

式中,$\boldsymbol{y}_s$ 是位置 s 处特征矢量。聚类过程从随机均值 $\boldsymbol{\mu}_k$ 开始迭代完成。

3.3 入射角效应按类校正

图像退化过程通常可由线性模型来描述(Beckers 等,1994),假设 y^r 为标记为 k 的区域 Ω_k 上的观测 SAR 海冰强度,z^r 为标记为 k 的区域 Ω_k 上的真实 SAR 海冰强度,两者的关系有

$$y^r = z^r m^r + a^r \tag{3}$$

式中,m^r 和 a^r 分别是标记为 x_v^r 的区域强度乘性退化因子和加性退化因子。

对退化模型取逆,z^r 的估计值 $\tilde{z}^r$ 为

$$\tilde{z}^r = y^r (\tilde{m}^r)^{-1} + (\tilde{a}^r)^{-1} \tag{4}$$

这里

$$(\tilde{m}^r)^{-1} = \frac{1}{m^r} \text{且} (\tilde{a}^r)^{-1} = -\frac{a^r}{m^r} \tag{5}$$

由于入射角效应只出现在距离向 j,因此校正是 1 维的,按像素取观测区域 Ω 上 y^r 沿方位向 i 的均值:

$$\bar{y}^r(j) = \frac{1}{N_j} \sum_{i \in \Omega} y^r(i, j) \tag{6}$$

式中,N_j 是区域 Ω 中第 j 列海冰像素的数量。

标记化后的分割区域在粗糙度和冰的含水量

上具有同质性，入射角效应在距离向引入的强度变化是位置的平滑变化函数，因此乘性和加性退化因子可由平滑变化的二阶多项式建模。

$$(\tilde{a}^{\mathrm{r}})^{-1}(j) = \sum_{q=0}^{2} a_q \frac{j^q - b_q}{c_q} \tag{7}$$

$$(\tilde{m}^{\mathrm{r}})^{-1}(j) = \sum_{q=0}^{2} m_q \frac{j^q - d_q}{e_q} \tag{8}$$

式中，b_q 和 d_q 为中和参数，c_q 和 e_q 为规格化参数，参数求解过程参见附录；a_q 和 m_q 是待优化的多项式系数。

任意图像区域的信息 I 都可由 Shannon 熵 H 定量表示（Applebaum，1996）。

$$I[\tilde{z}^{\mathrm{r}}(j)] = H[\tilde{z}^{\mathrm{r}}(j)] = -\sum_{w} p(w) \log p(w) \tag{9}$$

式中，$p(w)$ 是强度值为 w 的像素点在 $\tilde{z}^{\mathrm{r}}(j)$ 中出现的概率。假设最优系数 a_{o} 和 m_{o} 分别定义了最优因子 $\tilde{m}_{\mathrm{o}}^{-1}(j)$ 和 $\tilde{a}_{\mathrm{o}}^{-1}(j)$，则利用 Powell 的多维方向集方法和 Brent 1 维最优算法（Press 等，1992）可以找出最优加性系数 a_{o} 和乘性系数 m_{o}

$$\{a_{\mathrm{o}}, m_{\mathrm{o}}\} = \arg\min_{\{a,m\}} \left\{ I\left[\tilde{y}(j)(\tilde{m}^{\mathrm{r}})^{-1}(j) + (\tilde{a}^{\mathrm{r}})^{-1}(j) \right] \right\} \tag{10}$$

由最优参数 a_{o} 和 m_{o} 求出最优 1 维校正因子 $(\tilde{a}^{\mathrm{r}})^{-1}(j)$ 和 $(\tilde{m}^{\mathrm{r}})^{-1}(j)$，并扩展到 2 维校正因子 $(\tilde{a}^{\mathrm{r}})^{-1}$ 和 $(\tilde{m}^{\mathrm{r}})^{-1}$，$(\tilde{a}^{\mathrm{r}})^{-1}$ 中的每一行都与 $(\tilde{a}^{\mathrm{r}})^{-1}(j)$ 相同，$(\tilde{m}^{\mathrm{r}})^{-1}$ 中的每一行都与 $(\tilde{m}^{\mathrm{r}})^{-1}(j)$ 相同。利用式（4）即可计算出 z^{r} 的最优估计 $\tilde{z}_{\mathrm{o}}^{r}$。最后，基于校正后的结果重新计算区域特征矢量 $\boldsymbol{y}_v$。

3.4 区域合并

经过冰类校正的图像仍存在过多的分割区域，且在邻近区域间还有各种残存的不确定性；此外，在大范围 SAR 海冰监测中，人们更关注的是冰类的大尺度结构，因此区域合并是必须的。

假设每一类中各个小区域的图像值服从多元高斯分布（Press 等，2007），则最优分割 $x_{\mathrm{o}}^{\mathrm{r}}$ 可通过对以下成本函数最小化获得：

$$x_{\mathrm{o}}^{\mathrm{r}} = \arg\min_{x^{\mathrm{r}} \in X^{\mathrm{r}}} E_f \tag{11}$$

式中，E_f 是特征模型能量，定义如下：

$$E_f = \frac{1}{2} \sum_{k=1}^{n} \sum_{S_y \subseteq \Omega_k} \sum_{s \in S_y} \left\{ \log\left(\left| \sum\nolimits_k \right| \right) + (\tilde{z}_{\mathrm{os}}^{\mathrm{r}} - \boldsymbol{\mu}_k)^{\mathrm{T}} \sum\nolimits_k^{-1} (\tilde{z}_{\mathrm{os}}^{\mathrm{r}} - \boldsymbol{\mu}_k) \right\} \tag{12}$$

式中，$\tilde{z}_{\mathrm{os}}^{\mathrm{r}}$ 是 $\tilde{z}_{\mathrm{o}}^{\mathrm{r}}$ 在位置 s 处的特征矢量；S_v 是每个分割区域 v 中的各个位置，v 是区域 $\boldsymbol{\Omega}_k$ 的一部分；$\sum_k$ 是类 k 的协方差矩阵，$\boldsymbol{\mu}_k$ 是类 k 的均值。

基于式（11），利用卢洁等（2011）提出的方法，完成对所有节点的标记寻优，然后针对具有相同类的所有邻近区域对，以贪婪方式实现区域合并，并更新 RAG。

在区域合并完成时，分割算法将返回到 3.3 节，直到达到期望的迭代数，此时产生最终的分割。

3.5 评价标准

整体准确率和 Kappa 系数（Richards 等，2006）是两种常用的分割精度测量方法。整体准确率是像素正确标记的百分比。在计算 Kappa 系数之前，需要重新标记分割结果，使其与地面实况图像标记匹配，即 Kappa 系数是在整体准确率最大化情形下，利用下式获得的

$$k = \frac{P(A) - P(E)}{1 - P(E)} \tag{13}$$

式中，$P(A)$ 为观测一致率，$P(E)$ 为期望一致率。Kappa 系数的范围为 $[-1, 1]$。当 $k = 0$ 时，分割结果与随机分配的结果相当；当 k 为负时，分割结果相对于正确分割有较大偏差，k 值越大，分割结果越好，当 $k = 1$ 时，分割结果是完美的。

4 实验结果及分析

为模拟所提方法对入射角效应的适应能力，将每幅海冰场景划分为 3 个相等区段。图 3（a）是巴芬湾海冰 SAR 图像，实验图像分辨率为 882×1730，区段分辨率为 294×1730。图 4（a）是波斯尼亚湾海冰 SAR 图像，实验图像分辨率为 615×938，区段分辨率为 205×938。

基于整体准确率和 Kappa 系数，针对上述两组图像，把本文方法的分割结果与区域 MRF 方法的分割结果进行了比较。巴芬湾实验及区段 SAR 海冰图像的分割精度如表 2 所示，观察可知，对区段图像而言，基于区域 MRF 的分割所获整体准确率最高可达 89.93%，而本文方法对整体准确率的改进最高为 2.26%（92.19%—89.93%），Kappa 系数的提高为 0.0272（0.9087—0.8815）。然而对实验分辨率图像而言，由于入射角效应和其他非平稳因素的影响增大，区域 MRF 的整体准确率下降到 73.84%，但本文方法则将整体准确率提高到 80.64%，差异为 6.8%，Kappa 系数从 0.7188 提高到 0.7824，变化为 0.0636，精度得到明显改进。

在表3所示的波斯尼亚湾实验及区段SAR海冰图像的分割精度中也可以观察到同样现象。不同的是,对区段图像而言,本文方法对整体准确率的改进最高仅为1.78%(95.50%—93.72%),对应的Kappa系数的提高只有0.0169(0.9313—0.9144),低于巴芬湾的改进幅度。但对实验分辨率图像而言,本文方法对整体准确率的改进为8.23%(86.83%—78.60%),Kappa系数的变化为0.0865(0.8502—0.7637),精度改进的幅度高于巴芬湾。

此外,比较表2和表3可知,无论是实验分辨率图像,还是区段图像,一般来说,波斯尼亚湾的整体准确率和Kappa系数都要高于巴芬湾,可能的原因是波斯尼亚湾海冰分布对应的入射角范围小于巴芬湾海冰分布入射角范围。

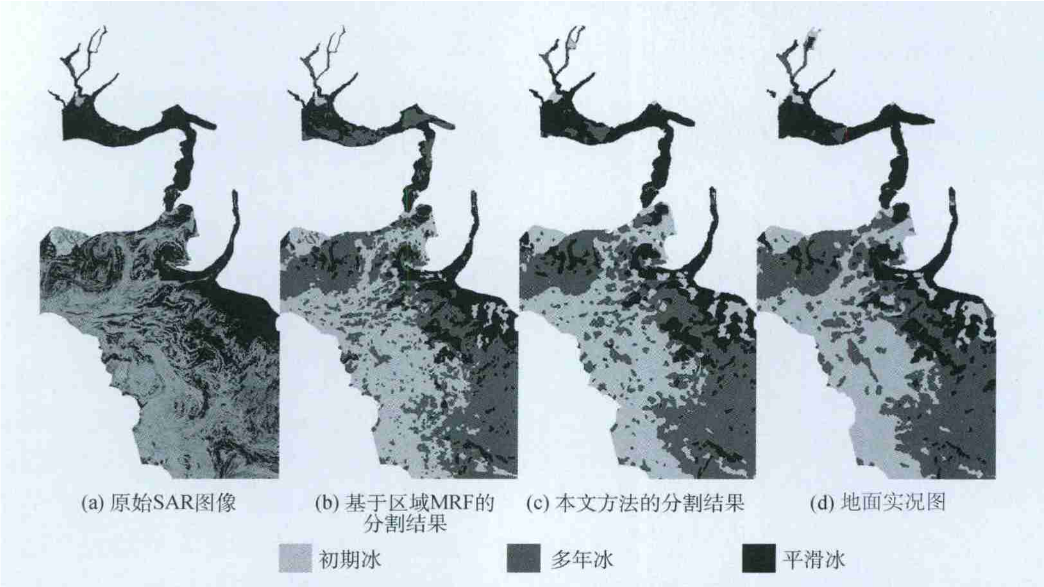

图3 巴芬湾SAR海冰图像分割结果

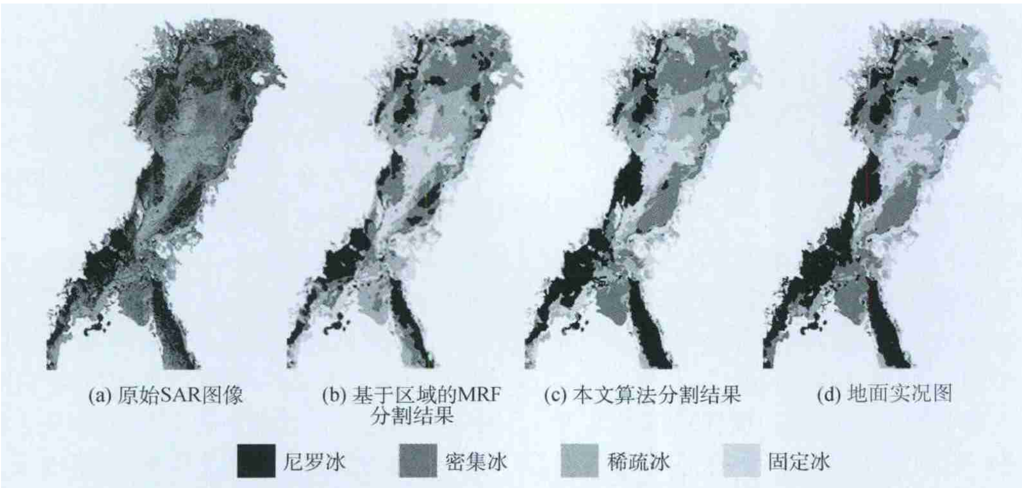

图4 波罗的海的波斯尼亚湾的SAR海冰图像分割结果

表2 实验及区段巴芬湾SAR海冰图像分割准确性比较

分辨率	基于区域MRF分割的整体准确率/%	本文方法的整体准确率/%	基于区域MRF分割的Kappa系数	本文方法的Kappa系数
882×1730	73.84	80.64	0.7188	0.7824
左294×1730	80.81	81.33	0.7992	0.8016
中294×1730	89.93	92.19	0.8815	0.9087
右294×1730	88.17	90.38	0.8623	0.8863

表 3 实验及区段波斯尼亚湾 SAR 海冰图像分割准确性比较

分辨率	基于区域 MRF 分割的整体准确率/%	本文方法的整体准确率/%	基于区域 MRF 分割的 Kappa 系数	本文方法的 Kappa 系数
615 × 938	78.60	86.83	0.7637	0.8502
左 205 × 938	92.06	93.61	0.9082	0.9228
中 205 × 938	93.72	95.50	0.9144	0.9313
右 205 × 938	85.82	85.88	0.8471	0.8478

针对巴芬湾海冰 SAR 图像,基于区域 MRF 的分割结果(图 3(b))显示出更多的歧义性,特别是在中、右区段,而本文方法(图 3(c))在这些区域则较好地兼顾了边缘定位和区域一致性。针对波斯尼亚湾海冰 SAR 图像,与基于区域 MRF 的分割结果(图 4(b))相比,经本文算法获得的结果(图 4(c))具有更好的区域连通性,图像中孤立区域明显减少,更接近地面实况图,特别是在左、中区段。这些观察都与表 2 和表 3 中的数据结果相一致。

可见,本文提出的算法通过集成入射角效应按类校正步骤,能够有效平滑同类海冰像素的强度值,提高了分割精度,然而随着入射角范围的增加,改进的幅度有所降低。

5 结论与展望

宽观测带(如 ScanSAR 技术)是业务化海冰监测的常用模式。入角度效应是 ScanSAR 模式海冰图像自动分割的主要障碍。本文提出的方法经由像素到区域再到大尺度区域这一途径,在区域增长迭代中组合了入射角效应校正步骤。经由对两幅不同的 ScanSAR 海冰图像的实验表明,本文算法能有效地提高宽观测带 SAR 海冰图像的分割精度,适合于完成 ScanSAR 模式下的非监督低级分类任务。

另外,作为一种类尺度特征,第一次组合迭代中获得的最优系数 a_o 和 m_o,反映了相同冰类沿距离向均值强度的变化趋势,而已有的研究已经证明这种变化趋势(入射角效应)与冰类有关,因此在未来的研究中我们将在高级分类中验证这种特征对增强各类海冰识别能力的有效性。

参考文献(References)

Agnew T and Howell S. 2003. The use of operational ice charts for evaluating passive microwave ice concentration data. Atmosphere-Ocean, 41(4): 317 – 331 [DOI: 10.3137/ao.410405]

Applebaum D. 1996. Probability and Information: An Integrated Approach. Cambridge: Cambridge University Press: 97

Beckers A L D, de Bruijn W C, Gelsema E S, Cleton-Soteman M I and van Eijk H G. 1994. Quantitative electron spectroscopic imaging in bio-medicine: methods for image acquisition, correction and analysis. Journal of Microscopy, 174(3): 171 – 182 [DOI: 10.1111/j.1365 – 2818.1994.tb03465.x]

Cavalieri D J, Parkinson C L, Gloersen P, Comiso J C and Zwally H J. 1999. Deriving long-term time series of sea ice cover from satellite passive-microwave multisensor data sets. Journal of Geophysical Research, 104 (C7): 15803 – 15814 [DOI: 10.1029/1999JC900081]

Clausi D A, Qin K, Chowdhury M S, Yu P and Maillard P. 2010. MAGIC: MAp-Guided Ice Classification system for operational analysis. Canadian Journal of Remote Sensing, 36(1): S13 – S25 [DOI: 10.1109/PRRS.2008.4783172]

Johannessen O M, Bengtsson L, Miles M W, Kuzmina S I, Semenov V A, Alekseev G V, Nagurnyi A P, Zakharov V F, Bobylevv L P, Pettersson L H, Hasselmann K and Cattle H P. 2004. Arctic climate change: observed and modelled temperature and sea-ice variability. Tellus-Series A-Dynamic Meteorology and Oceanography, 56(4): 328 – 341 [DOI: 10.1111/j.1600 – 0870.2004.00060.x]

Johannessen O M, Alexandrov V, Frolov I Y, Sandven S, Pettersson L H, Bobylev L P, Kloster K, Smirnov V G, Mironov Y U and Babich N G. 2007. Remote Sensing of Sea Ice in the Northern Sea Route: Studies and Applications. Chichester: Springer-Praxis Publishing.

Karvonen A J. 2004. Baltic Sea ice SAR segmentation and classification using modified pulse-coupled neural networks. IEEE Transactions on Geoscience and Remote Sensing, 42(7): 1566 – 1574 [DOI: 10.1109/TGRS.2004.828179]

卢洁,杨学志,郎文辉,左美霞,徐勇. 2011. 区域 GMM 聚类的 SAR 图像分割. 中国图象图形学报,16(11): 2088 – 2094

马闯关,吴有新,史开,刘大刚. 2011. 因特网上高纬冰况信息资料的辨识. 航海技术,(2): 16 – 18

Mäkynen M P, Manninen A T, Similä M H, Karvonen A J and Martti T H. 2002. Incidence angle dependence of the statistical properties of C-Band HH-Polarization backscattering signatures of the Baltic sea ice. IEEE Transactions on Geoscience and Remote Sensing, 40(12): 2593 – 2605 [DOI: 10.1109/TGRS.2002.806991]

Oliver C and Quegan S. 2004. Understanding Synthetic Aperture Radar Images. Raleigh: SciTech Publishing Inc: 197

Peter Y. 2010. Segmentation of RADARSAT-2 Dual-Polarization Sea Ice Imagery. Waterloo: University of Waterloo: 19 – 20

Press W H, Flannery B P, Teukolsky S A, and. Vetterling W T 1992. Numerical Recipes in C, the Art of Scientific Computing 2nd ed. Cambridge: Cambridge University Press: 402 - 419

Press W H, Teukolsky S A, Vetterling W T and Flannery B P. 2007. Numerical Recipes: the Art of Scientific Computing 3rd edn. Cambridge: Cambridge University Press: 842

Richards J A and Jia X P. 2006. Remote Sensing Digital Image Analysis. Berlin Heidelberg: Springer-Verlag: 304 - 305

Soh L K, Tsatsoulis C, Gineris D and Bertoia C. 2004. ARKTOS: An intelligent system for SAR sea ice image classification. IEEE Transactions on Geoscience and Remote Sensing, 42(1): 229 - 248 [DOI: 10.1109/TGRS.2003.817819]

Wilson K J, Falkingham J, Melling H and Abreu R D. 2004. Shipping in the Canadian Arctic: other possible climate change scenarios // Proceedings of the IEEE International Geoscience and Remote Sensing Symposium, Honolulu, Hawaii: IEEE, 3: 1853 - 1856 [DOI: 10.1109/IGARSS.2004.1370699]

Yu Q Y and Clausi D A. 2007. SAR sea ice image analysis based on iterative region growing using semantics. IEEE Transaction on Geoscience and Remote Sensing, 45(12): 3919 - 3931 [DOI: 10.1109/TGRS.2007.908876]

附录 A

针对给定图像 $\bar{y}^{\mathrm{r}}(j)$,为了中和校正因子$(\tilde{m}^{\mathrm{r}})^{-1}(j)$和$(\tilde{a}^{\mathrm{r}})^{-1}(j)$的全局转换效果,引入均值保护条件

$$\sum_{j\in\boldsymbol{\Omega}}\bar{y}^{\mathrm{r}}(j) = \sum_{j\in\boldsymbol{\Omega}}\left(\bar{y}^{\mathrm{r}}(j)(\tilde{m}^{\mathrm{r}})^{-1}(j) + (\tilde{a}^{\mathrm{r}})^{-1}(j)\right) \tag{A1}$$

为满足上述条件,把加性因子的均值设置为 0

$$\sum_{j\in\boldsymbol{\Omega}}(\tilde{a}^{\mathrm{r}})^{-1}(j) = 0 \tag{A2}$$

因此乘性因子应满足

$$\sum_{j\in\boldsymbol{\Omega}}\bar{y}^{\mathrm{r}}(j) = \sum_{j\in\boldsymbol{\Omega}}\bar{y}^{\mathrm{r}}(j)(\tilde{m}^{\mathrm{r}})^{-1}(j) \tag{A3}$$

由式(7)和式(A2)得到

$$\sum_{j\in\boldsymbol{\Omega}}\left(\sum_{q=0}^{2}a_q\frac{j^q - b_q}{c_q}\right) = 0 \tag{A4}$$

由式(8)和式(A3)得到

$$\sum_{j\in\boldsymbol{\Omega}}\bar{y}^{\mathrm{r}}(j) = \sum_{j\in\boldsymbol{\Omega}}\bar{y}^{\mathrm{r}}(j)\left(\sum_{q=0}^{2}m_q\frac{j^q - d_q}{e_q}\right) \tag{A5}$$

首先为了求解式(A4),将 a_0 设置为中性值 0

$$\sum_{j\in\boldsymbol{\Omega}}\left(\sum_{q=1}^{2}a_q\frac{j^q - b_q}{c_q}\right) = \sum_{q=1}^{2}\frac{a_q}{c_q}\sum_{j\in\boldsymbol{\Omega}}(j^q - b_q) = 0 \tag{A6}$$

$a_q\neq 0$ 且 $c_q\neq 0$ 时上式有非平凡解,此时 $q = 1,2$

$$\sum_{j\in\boldsymbol{\Omega}}(j^q - b_q) = 0 \tag{A7}$$

得到

$$b_q = \frac{1}{S}\sum_{j\in\boldsymbol{\Omega}}j^q \tag{A8}$$

这里 $S = \sum_{j\in\boldsymbol{\Omega}}1$ 是 $\bar{y}^{\mathrm{r}}(j)$ 中属于 $\boldsymbol{\Omega}$ 的像素数。

类似地,通过把 m_0 设置为中性值 1 得到

$$d_q = \sum_{j\in\boldsymbol{\Omega}}\bar{y}^{\mathrm{r}}(j)j^q \Big/ \sum_{j\in\boldsymbol{\Omega}}\bar{y}^{\mathrm{r}}(j) \tag{A9}$$

为保证多项式系数的相同变化能产生等值的强度变化,我们对参数做规格化处理

$$\frac{1}{S}\sum_{j\in\boldsymbol{\Omega}}\left|\bar{y}^{\mathrm{r}}(j)\frac{j^q - d_q}{e_q}\right| = 1 \tag{A10}$$

得到

$$e_q = \frac{1}{S}\sum_{j\in\boldsymbol{\Omega}}\left|\bar{y}^{\mathrm{r}}(j)(j^q - d_q)\right| \tag{A11}$$

类似地可以得到

$$c_q = \frac{1}{S}\sum_{j\in\boldsymbol{\Omega}}\left|j^q - b_q\right| \tag{A12}$$